

## Full Length Article

## Excellent strength-ductility synergy in metastable high entropy alloy by laser powder bed additive manufacturing

P. Agrawal<sup>a</sup>, S. Thapliyal<sup>a</sup>, S.S. Nene<sup>a</sup>, R.S. Mishra<sup>a,\*</sup>, B.A. McWilliams<sup>b</sup>, K.C. Cho<sup>b</sup><sup>a</sup> Center for Friction Stir Processing, Department of Materials Science and Engineering, University of North Texas, Denton, TX, 76203, USA<sup>b</sup> Weapons and Materials Research Directorate, U.S. Army Research Laboratory, Aberdeen Proving Grounds, Aberdeen, MD, 21005, USA

## ARTICLE INFO

## Keywords:

Powder bed fusion  
Additive manufacturing  
High entropy alloys  
Transformation induced plasticity  
Twinning

## ABSTRACT

High entropy alloys (HEAs) have attracted scientific interest due to their good mechanical properties and failure resistance, whereas additive manufacturing (AM) has emerged as a powerful yet flexible processing route for advanced materials. However, limitations inherent in both these fields include HEAs displaying inferior mechanical properties in as cast condition; and AM demands expansion of printable alloys. A new metastable  $\text{Fe}_{40}\text{Mn}_{20}\text{Co}_{20}\text{Cr}_{15}\text{Si}_5$  (CS-HEA) HEA showing stabilized  $\epsilon$ -h.c.p. dominated microstructure after laser powder bed fusion additive manufacturing has been evaluated. As-printed CS-HEA showed higher strength due to high work hardenability, whereas substantial uniform ductility is associated with a combination of transformation and twinning induced plasticity during deformation. Additionally, very low volume percent of voids ( $\sim 0.1\%$ ) along with high strength-ductility shows excellent printability of the CS-HEA using laser-based additive manufacturing.

## 1. Introduction

Laser powder bed fusion (LPBF) additive manufacturing (AM) is a disruptive technology that promises to change how complex shaped products are fabricated. LPBF offers benefits such as fabrication of complex shapes without requiring long supply chain networks, minimal-waste production, and product customization [1]. Despite these advantages, LPBF is currently hindered by limited choice of structural printable materials. Furthermore, most of the materials investigated display a notable fraction of process-induced defect density, which is further minimized by post-printing treatments to meet properties similar to conventionally-processed materials [2]. By process induced defects we mean voids or cracks, both of which can act as stress raisers that induce abrupt/sudden failure of the material during service. These shortcomings limit the application of LPBF for structural applications in aerospace, automotive, marine and infrastructure sections.

To solve the problem of lack of printable structural materials, efforts have been put forth to develop new alloys and/or to modify conventional alloys for AM [3,4]. Of specific interest is LPBF AM of high entropy alloys (HEAs), as they offer good strength-ductility combinations, corrosion resistance, and microstructural flexibility [5]. Furthermore, HEAs may provide a vast number of new alloys for specific application-based alloy development for AM [6]. Brif *et al.* [7] studied the  $\text{FeCoCrNi}$  HEA alloy prepared by selective laser melting technology, which

showed single-phase as-printed microstructure with good strength and ductility combination. Similarly, phase evolution and mechanical properties of AM-processed  $\text{AlCoCrFeNi}$  and  $\text{CoCrFeMnNi}$  have also been reported. Kuwabara *et al.* [8] observed that mechanical properties of  $\text{AlCoCrFeNi}$  in the build direction are better than those in the direction perpendicular to build. Piglione *et al.* [9] observed solidification microstructure of the  $\text{CoCrFeMnNi}$  HEA and confirmed that microstructure in the printed alloy is governed by epitaxial growth and competitive grain growth. With this background, clearly researchers are endeavoring to expand the pool of printable materials for AM using the high entropy alloy design approach. Limited studies are available that report on the design of materials for LPBF concentrating on the combination of high strength and ductility despite the presence of voids. Since in any powder-based AM process the formation of such processing defects is inevitable, a novel approach of alloy design is essential to develop a microstructure in which the presence of such defects has a limited effect on the mechanical properties of the material.

Li *et al.* [10] introduced and Nene *et al.* [11] further extended the design of a metastable HEA, wherein they suggested that extensive work hardening can be achieved in the material by reducing matrix phase stability and triggering transformation induced plasticity. The key parameter to ensure this decreased phase stability is tuning the stacking fault energy (SFE) of the matrix phase [12,13]. SFE of the matrix phase can be engineered by selection of particular alloy

\* Corresponding author.

E-mail address: [Rajiv.Mishra@unt.edu](mailto:Rajiv.Mishra@unt.edu) (R.S. Mishra).

chemistry such that it increases the driving force ( $\Delta G^{\gamma \rightarrow \epsilon}$ ) for the  $\gamma \rightarrow \epsilon$  transformation, which is indirectly related with the matrix SFE [14,15]. To achieve this, Nene et al. [16] added Cr and Si in Fe-Mn rich alloy to tune the  $\Delta G^{\gamma \rightarrow \epsilon}$  values, which can thus indirectly reduce the SFE of the  $\gamma$  matrix, thereby making it more metastable. This pronounced increase in metastability triggered the transformation induced plasticity (TRIP) effects. Metastability has also been used to improve fatigue properties of the material which involves localized crack nucleation and growth.  $\gamma \rightarrow \epsilon$  transformation provides localized work hardening in the vicinity of nucleated fatigue cracks and thus delays crack propagation by transformation induced crack retardation, thereby providing good fatigue resistance to these new alloys [17]. The design of metastable HEAs provides an opportunity to develop damage tolerant alloys for LPBF AM, since multiple deformation mechanisms can be activated selectively based on stress concentration in the vicinity of voids or cracks, thereby promoting localized work hardening [18].

The present study attempts to use the benefit of metastability-based alloy design to investigate a new printable alloy using LPBF. A metastable Fe<sub>40</sub>Mn<sub>20</sub>Co<sub>20</sub>Cr<sub>15</sub>Si<sub>5</sub> (CS-HEA) was selected for printing using the LPBF AM process. The design strategy for the CS-HEA has been explained previously [11,12,16]. As-printed microstructure and tensile properties are compared with its conventionally as-cast condition. A brief explanation of the plasticity in the vicinity of the voids is also reported.

## 2. Experimental

The AM specimens were manufactured from pre-alloyed, gas-atomized Fe<sub>40</sub>Mn<sub>20</sub>Co<sub>20</sub>Cr<sub>15</sub>Si<sub>5</sub> (at. %) powder having chemical composition as provided in Table 1. The average size of powder particles was  $45 \pm 15 \mu\text{m}$ . A LPBF system Aconity MIDI (Aconity 3D GmbH) equipped with a single (maximum 1000 W) fiber laser was used for printing a 30 mm long, 15 mm wide, 4 mm thick CS-HEA specimen. For printing of CS-HEA laser power, hatch spacing, layer thickness, scanning speed and the rotation between adjacent layers used are 140 W, 0.1 mm, 0.04 mm, 800 mm/sec and 67° respectively. Printing was carried out in the protective atmosphere of argon, with the O<sub>2</sub> content below 0.01 % throughout the LPBF process. As-cast CS-HEA samples were used as reference materials to compare the mechanical properties and microstructural evolution with as-printed specimens. Casting procedure is reported in our earlier work on CS-HEA [16].

Microstructure of the alloy in as-printed and as-cast conditions were analyzed by various methods. Samples for microstructural analysis were machined using electron discharge machine (EDM) then mechanically polished till 0.02 colloidal silica to get a mirror surface finish. X-ray diffraction (XRD) measurements were performed using an RIGAKU Ultima III X-Ray equipped with Cu K<sub>α</sub> ( $\lambda = 0.154 \text{ nm}$ ) radiation operated at 40 kV and 44 mA. The composition of the sample was characterized using scanning electron microscopy ESEM FEI Quanta 200 equipped with energy dispersive spectroscopy (EDS) detector. The operating voltage for compositional analysis was 20 kV with a beam current of 6.1 nA and the working distance of 10 mm. X-ray microscopy (XRM) of the as-printed sample was performed using Zeiss Xradia Versa 520 microscope. The scan voltage and power for XRM were set to 160 kV and 10 kW, respectively; the binning value was set to 1. Sample volume of  $4.0 \times 1.5 \times 1 \text{ mm}^3$  from as-printed condition was scanned; the voxel size was set to  $\sim 1.9 \mu\text{m}$ . Image analysis of the 3D reconstructed image was performed using Dragon fly software to

determine the volume fraction and the spatial distribution of voids within the sample. Electron backscattered diffraction (EBSD) scans were done on FEI Nova NanoSEM230 with Hikari EBSD camera attachment operating at 20 kV and 6.1 nA current and 75 nm step size using a pre-tilt holder. The EBSD data was analyzed using TSL OIM 8 software. Dislocation density measurements were made using TSL software. Rectangular 1 mm-thick, dog-bone-shaped mini-tensile specimens were electron discharge machined. Gage length and width of the tensile specimens were 5 and 1.0 mm, respectively. In each condition, three samples were tested at room temperature and an initial strain rate of  $10^{-3} \text{ s}^{-1}$  to confirm reproducibility of the results.

## 3. Results and discussion

Figs. 1(a) and (b) show the backscattered image and EBSD inverse pole figure (IPF) of as-printed sample on the surface parallel to the build direction, respectively. Fig. 1(c) presents sample orientation with respect to build direction. The XRD pattern (Fig. 1(d)) and phase map (Fig. 1(e)) of as-printed material show  $\epsilon$  phase dominated (~72 %) dual phase microstructure having 28 % retained  $\gamma$  phase. This is in accordance with the fact that simultaneous addition of Cr and Si decreases the  $\Delta G^{\gamma \rightarrow \epsilon}$  for  $\epsilon$  formation (i.e., increase the  $\gamma$  phase metastability) and hence increases the feasibility for obtaining  $\epsilon$ -rich microstructure at room temperature. Moreover, our earlier work [16] on CS-HEA confirms that synergistic action of strain and temperature can stabilize  $\epsilon$  phase at room temperature, thereby giving flexible microstructural evolution. As a result, extreme metastability of  $\gamma$  phase along with high strain and rapid cooling during AM processing resulted in stabilization of  $\epsilon$ -dominated microstructure in as-printed condition. Equilibrium solidification of CS-HEA should result in dominance of  $\epsilon$  phase whereas rapid solidification may cause dual phase ( $\gamma + \epsilon$ ) microstructure [16]. Additive manufacturing (AM) is a layer by layer manufacturing process in which heat accumulation in the previously solidified layer occurs due to thermal cycling thereby prevailing formation of high temperature  $\gamma$  (FCC) phase in that layer. Thus, this thermal cycling effect which does not occur during conventional casting leads to the formation of different phase fractions in metastable CS-HEA even though the composition is same.

Along with phase stability, grain size and morphology are crucial to decide deformation response of the material under loading. Fig. 1(a) is a backscattered electron image of as-printed CS-HEA at lower magnification showing mixed grain morphology having dominance of columnar grains with an average grain size of  $30 \mu\text{m}$ . Generally, AM materials have columnar grains due to directional heat extraction during non-equilibrium solidification; i.e., columnar grains grow opposite to heat flux direction (towards the base plate) [19]. Whereas, equiaxed grain morphology forms owing to constitutional supercooling near the solidification front and heterogeneous nucleation on partially melted powders [3]. Microstructural evolution of the as-printed specimen was further compared with the as-cast condition. Consistent with the previous report,  $\epsilon$  preeminence is evident also with the XRD patterns for both conditions (Fig. 1(d)) show  $\epsilon$  peak ( $2\theta = 46.8^\circ$ ) as most intense peak irrespective of processing. Whereas the grain size in as-cast condition was about  $100 \mu\text{m}$  [16], which is significantly large as compared to as-printed condition ( $30 \mu\text{m}$ ).

Also, important to establish the level of elemental segregation in the printed sample (Fig. 1(g) 1–6)). Elemental composition depicted from the EDS map is very close to the nominal composition (Table 1) along

**Table 1**  
Chemical composition of the pre-alloyed powder.

Elements	Cr	Co	Si	Mn	Fe
At. (%) (Nominal)	15	20	5	20	40
At. (%) (Actual)	$14.8 \pm 1$	$19.1 \pm 1.16$	$5.5 \pm 0.4$	$18.8 \pm 1.08$	$41.8 \pm 1.10$

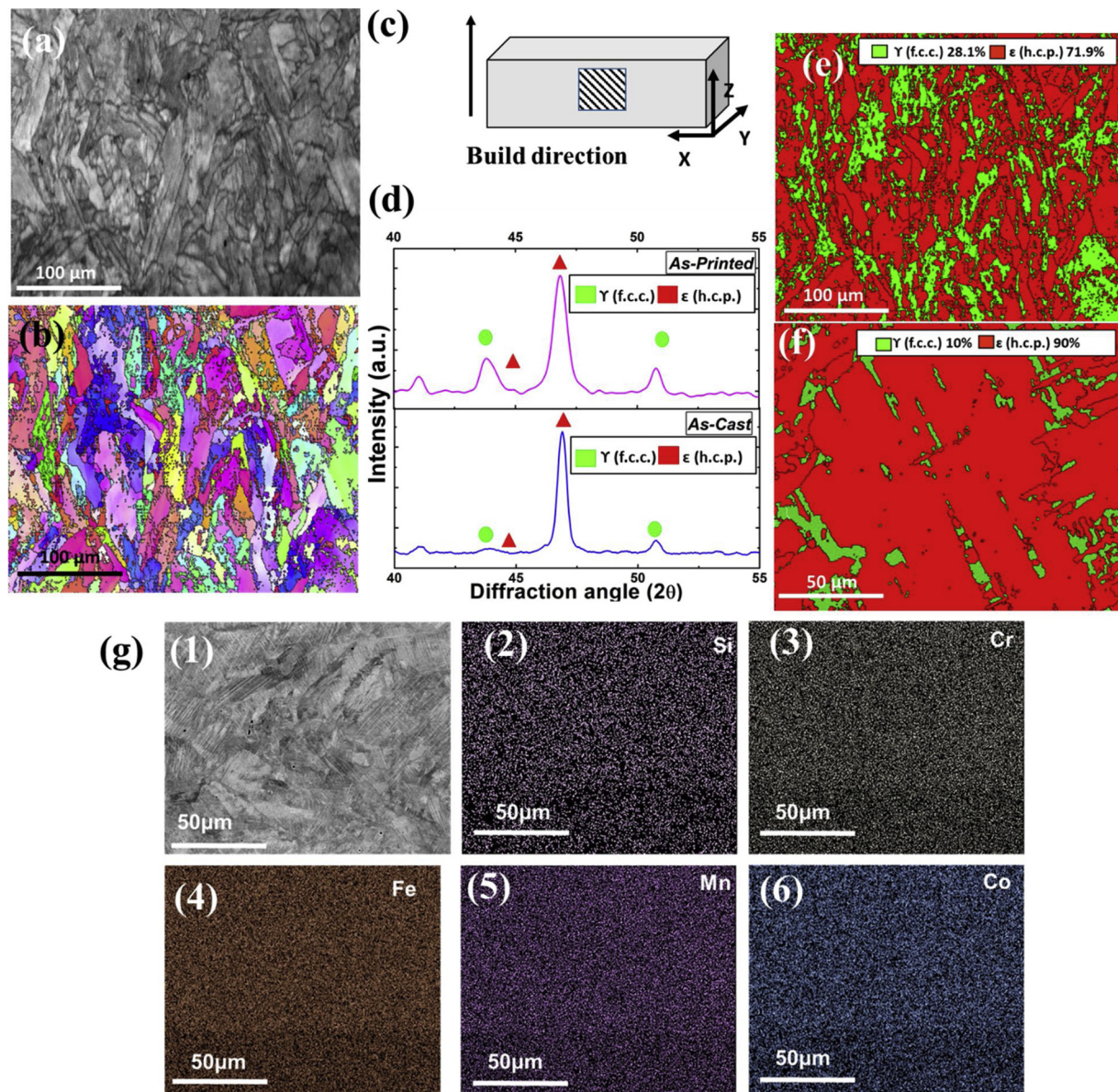


**Fig. 1.** Microstructural characterization of CS-HEA (a) BSE image and (b) IPF of as-printed sample, (c) schematic showing sample's orientation as compared to build direction, (d) XRD patterns of as-cast and as-printed conditions (e), (f) phase map of as-printed and as-cast sample respectively, and (g) EDS map of as-printed sample.

with uniform elemental distribution, which suggests that as-printed material does not have any noticeable macro-segregation.

Fig. 2(a) displays engineering stress – engineering strain curves for the as-printed and as-cast conditions. The difference in yield strength (YS) among these is attributed mainly to the difference in grain size. As-printed specimen exhibited YS of  $530 \pm 40$  MPa whereas as-cast specimen has YS of  $420 \pm 20$  MPa. The most interesting observation is the difference in work hardening ability, which provided as-printed condition with excellent strength-ductility combination. AM literature on conventional alloys claimed that as-printed AM tensile properties are always better than as-cast condition and much inferior to thermo-mechanically processed material [7,9,20,21]. The present work shows ultimate tensile strength ( $\sim 1.1$  GPa) and ductility (30 %) comparable with thermomechanically processed material [16] and much higher than the as-cast counterpart. Further, Fig. 2(b) shows fracture surface of the as-printed sample after tensile failure, Fig. 2(b)-1 shows the full view of failed sample and Fig. 2(b)-2 shows magnified view, which shows that the sample contains two types of features on fracture surface; void sheet (Fig. 2(b)-3) and quasi cleavage (Fig. 2(b)-4). Quasi

cleavage represents mixture of clean surface, tear lips and dimples whereas void sheet represents sheet of fine dimples. CS-HEA is a high work hardening (WH) rate material, when a high WH material deforms necking has been delayed. The flow stress of the material can reach to high value and causes plastic instability before necking. Hence there is no time for void nucleation and growth in necking [22].

Generally, AM materials are associated with processing defects such as voids and cracks, which act as stress raisers and undergo abrupt failure during service [21,23]. As-printed CS-HEA did not contain any cracks and contained very small void volume percent (vol%) of  $\sim 0.1$  %, as obtained from the reconstructed X-ray micrographs. The void vol % is measured as the ratio of total volume of voids in the scanned sample to the total volume of the scanned sample. However, note that these voids would have a minimum dimension of  $2\text{ }\mu\text{m}$  due to the set voxel size. Moreover, these voids were very small and uniformly distributed throughout the printed volume of the gage of the tensile sample (Fig. 2(c)). Such a low vol% of voids suggests extremely good printability of CS-HEA using 3D printing. The presence of voids or cracks was always reported to deteriorate the deformation response in

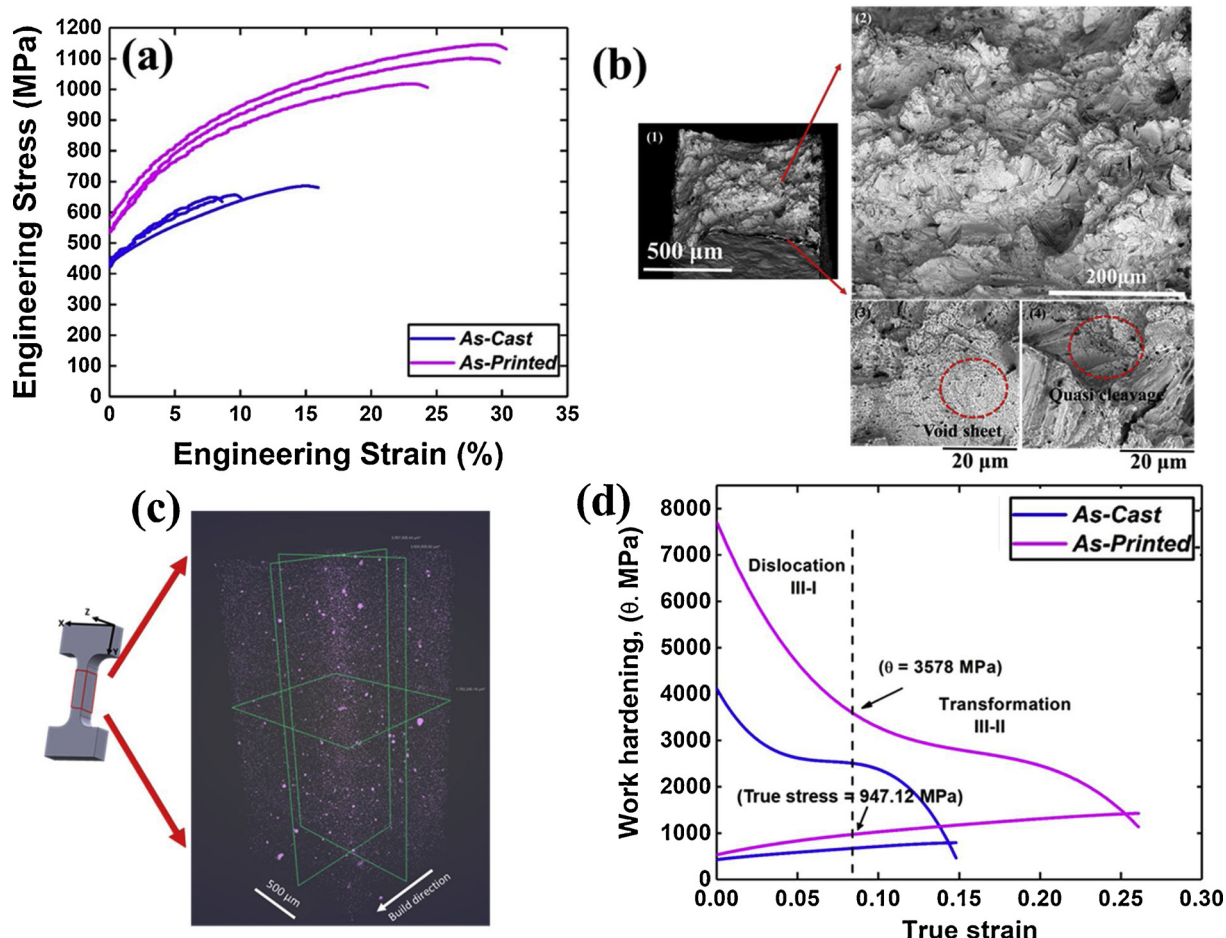


**Fig. 2.** Mechanical properties of CS-HEA. (a) Engineering stress-stain curve for two conditions, (b) SEM image of fracture surface of as-printed sample, (c) 3D XRM micrograph of as-printed sample, and (d) work hardening curve for two conditions.

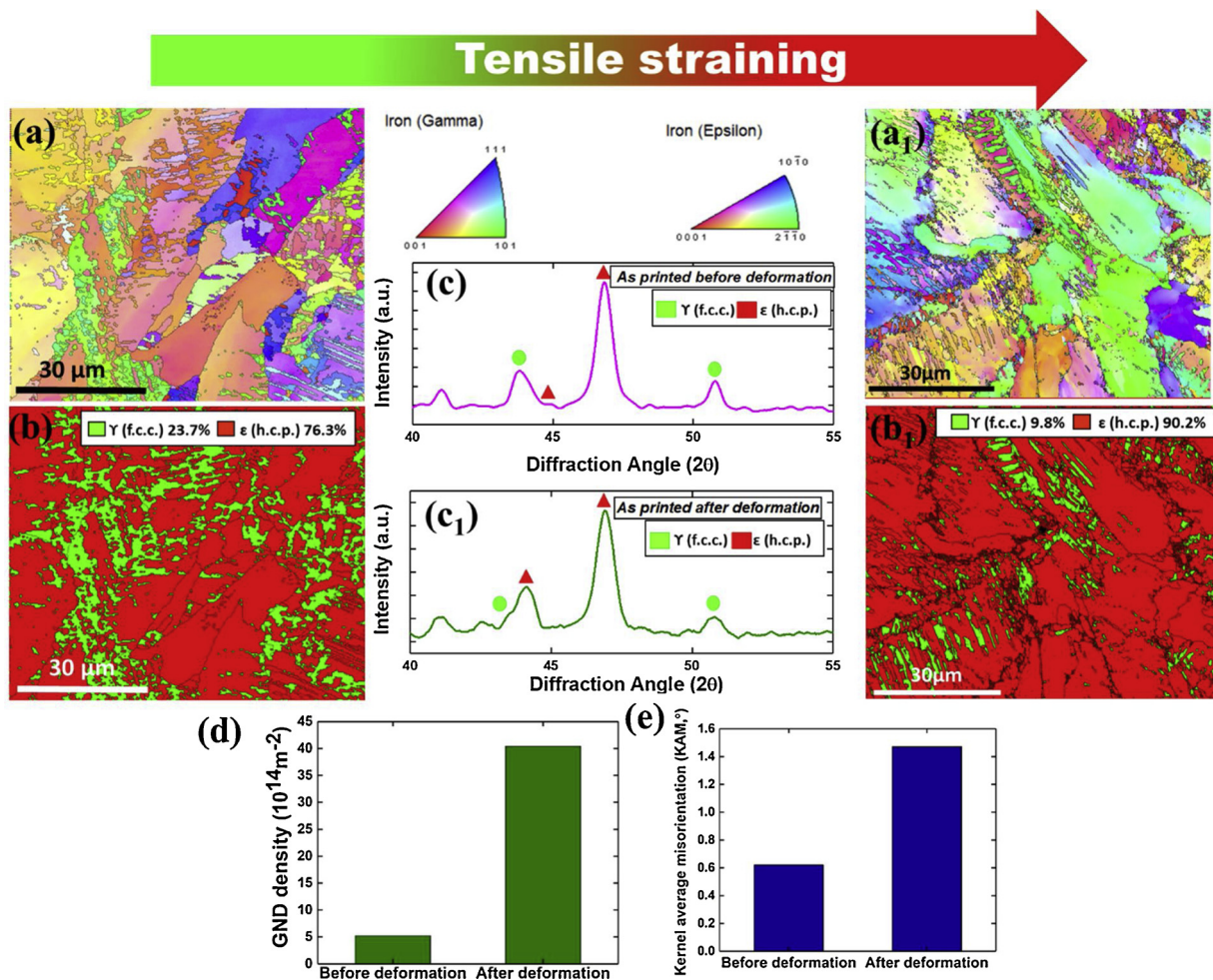
conventional materials, but CS-HEA showed exceptional tensile ductility despite the presence of these defects. The main reason for that is the uniform distribution of the voids and exceptionally good work hardenability of the material. As-printed material with high strain hardening exponent ( $n$ ) of  $\sim 0.29$  as compared with the as-cast sample ( $\sim 0.22$ ) reassures that as-printed material is more work hardenable.

Fig. 2(d) shows work hardening behavior of CS-HEA for as-printed condition (pink curve in Fig. 2(d)) and confirms the operation of Stage III during deformation. However, the clear indication of sustained work hardening in as-printed specimen over the strain range of 9%–21% is evident. The material was able to maintain WH rate of  $> 3000$  MPa up to almost 19 % strain, which is not commonly observed in any conventional f.c.c. or h.c.p. material with any processing history. This sustainment further divides the work hardening Stage III into two substages: substage III-I corresponding to slip dominated plasticity; and substage III-II corresponding to non-slip dominated plasticity [11,12].

A Stage III work hardening for as-printed sample shows a slope change at  $\theta = 3578$  MPa, which corresponds to change in work hardening mechanism. The values of engineering stress and strain corresponding to the change in controlling mechanism are 868 MPa (true stress = 947.12 MPa) and 0.077, respectively. Above 868 MPa, the deformation is believed to be controlled by non-slip assisted mechanisms such as TRIP in f.c.c. phase or twinning in h.c.p. phase [24–26]. Our earlier work on CS-HEA [16] suggested that it accommodates strain primarily with non-basal assisted plasticity if the microstructure is  $\epsilon$ -dominated. In line with this, as-printed CS-HEA specimen is  $\epsilon$ -dominated dual phase microstructure as mentioned before, and thus exhibited dual phase strengthening effect as suggested by the sustained

work hardening response during deformation [11,12].

Thus, in the as-printed specimen, deformation occurs mainly via uniform strain accommodation in both phases. Fig. 3(a–e) captures the deformation behavior of the as-printed HEA.  $\gamma$  phase accommodates strain via transformation induced plasticity, and is captured by the decrease of  $\gamma$  fraction from 28.1 in as-printed to 9.1 % at failure (Fig. 3(b, b<sub>1</sub>) and (c, c<sub>1</sub>)); whereas  $\epsilon$  phase accommodates strain mainly via non-basal activity, as suggested by higher value of  $< c + a >$  dislocation density after tensile deformation (Fig. 3(d)). To understand the deformation in  $\epsilon$  phase in CS-HEA, we performed detailed TEM as well as in-situ neutron diffraction analysis of friction stir processed CS-HEA [27] in our earlier work. According to in-situ neutron diffraction of as-friction stir processed CS-HEA specimens,  $\epsilon$  phase predominantly accommodated deformation during in-situ straining via substantial lattice reorientation, thus resulting in {10.3} contraction and {10.2} extension twinning along with  $< c + a >$  slip. The  $< c + a >$  slip in the  $\epsilon$  phase was attributed mainly to the lower  $c/a$  ratio ( $\sim 1.619$ ) of the h.c.p. unit cell before tensile deformation [27,28]. To verify a similar mechanism in as-printed CS-HEA, we estimated the  $c/a$  ratio of the as-printed specimen using XRD pattern (Fig. 1(d)) and it was  $\sim 1.618$ . This value of  $c/a$  ratio was significantly lower than the ideal value of 1.633 and very close to that for friction stir processed CS-HEA as estimated by x-ray as well as neutron diffraction. Moreover, the value of  $c/a$  ratio decreased to 1.593 after tensile deformation indicating significant compression of  $c$  axis and expansion of  $a$  axis during deformation in  $\epsilon$  phase, suggesting higher propensity of  $< c + a >$  slip for strain accommodation. This is consistent with our earlier results on fine grained CS-HEA which displayed reduction in  $c/a$  ratio from



**Fig. 3.** Microstructural evolution after deformation (a) and (a<sub>1</sub>) IPF map of as-printed sample before and after deformation, respectively; (b) and (b<sub>1</sub>) phase map before and after deformation, respectively; (c) and (c<sub>1</sub>) XRD before and after deformation respectively; (d)  $\langle c + a \rangle$  pyramidal slip GND density distribution for epsilon phase before and after deformation; (e) KAM distribution before and after deformation.

1.619 to 1.588 by in-situ neutron diffraction after tensile deformation [27,28].  $\langle c + a \rangle$  slip activity was further supported by the higher KAM values in  $\epsilon$  phase field along with significant increased  $\langle c + a \rangle$  geometrically necessary dislocation density in the  $\epsilon$ -h.c.p. phase for as-printed specimen after complete tensile deformation (Fig. 3(d) and (e)). As a result, lower  $c/a$  ratio enabled the  $\epsilon$  phase to accommodate larger strain via non-basal plasticity, thereby giving very high work harden ability to the as-printed alloy.

Fig. 4 [19,29–40] compares the as-printed CS-HEA with other commonly-used materials in AM. Alloys are compared based on their strength-ductility index (SDI) value, which is mathematically defined as  $(\text{UTS-YS}) \times \text{plastic strain}$  (engineering UTS value of all materials is used for calculating SDI). SDI is plotted as a function of total elongation for comparison of tensile properties of various materials to date using different AM routes for fabrication. This analysis indicated that, to date, CS-HEA outperforms all other AM materials on this basis. It also suggests that CS-HEA exhibits highest work hardening ability, which provided it with maximum tensile elongation among other materials. At present, stainless steels and Ti alloys are used as conventional high-strength printable materials, but CS-HEA turns out to be remarkably good in terms of deformation response. An average void vol% reported in high-strength materials is  $\sim 0.5\%$ , whereas CS-HEA displayed very low void vol% of  $0.1\%$ ; indicating good printability with laser powder bed additive manufacturing process.

#### 4. Conclusions

A metastable CS-HEA with minimal void vol% was successfully fabricated using LPBF AM technique. As-printed  $\epsilon$ -dominated columnar grained microstructure facilitated exceptional work hardening ability in CS-HEA, and thus resulted in very high strength-ductility synergy under tensile loading. The higher strength-ductility synergy is attributed mainly to uniform strain partitioning among  $\gamma/\epsilon$  phases due to pronounced transformation induced plasticity in  $\gamma$  grains and non-basal plasticity including twinning in  $\epsilon$  grains. The as-printed material not only showed improved mechanical properties in comparison with as-cast material, thereby showing highest SDI value among all printed high-strength materials. The highest SDI value with lowest void vol% makes CS-HEA a promising printable material using laser powder bed additive manufacturing process.

#### CRediT authorship contribution statement

**P. Agrawal:** Data curation, Formal analysis, Methodology, Writing - original draft. **S. Thapliyal:** Data curation, Writing - original draft. **S.S. Nene:** Data curation, Methodology, Writing - original draft. **R.S. Mishra:** Project administration, Resources, Supervision, Writing - review & editing. **B.A. McWilliams:** Project administration, Writing - review & editing. **K.C. Cho:** Project administration, Writing - review & editing.

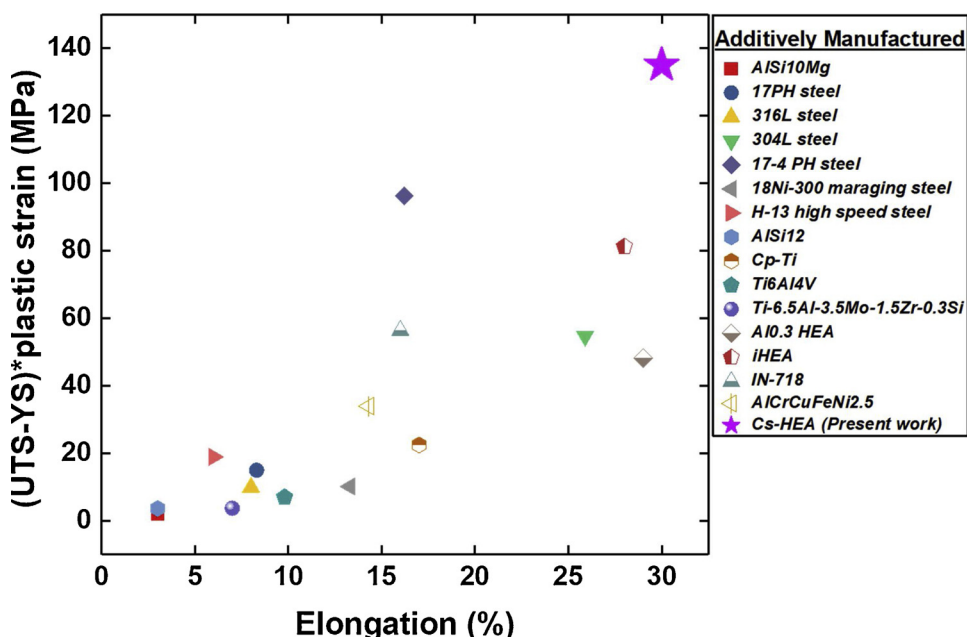


**Fig. 4.** Comparison of strength ductility index as a function of elongation for different additively manufactured alloys reported so far (engineering UTS value of all materials is used for calculating SDI) [19,29–40].

#### Declaration of Competing Interest

Authors have no conflict of interest.

#### Acknowledgements

This current study was performed under cooperation agreement between the Army Research Laboratory, USA and University of north Texas (W911NF1920011). The authors want to thank Center for Advanced Research and Technology for allowing access to microscopy facilities at the University of North Texas.

#### References

- [1] I. Paoletti, Mass customization with additive manufacturing: new perspectives for multi formative building components in architecture, *Procedia Eng.* 180 (2017) 1150–1159, <https://doi.org/10.1016/j.proeng.2017.04.275>.
- [2] S.K. Everton, M. Hirsch, P.I. Stavroulakis, R.K. Leach, A.T. Clare, Review of in-situ process monitoring and in-situ metrology for metal additive manufacturing, *Mater. Des.* 95 (2016) 431–445, <https://doi.org/10.1016/j.matdes.2016.01.099>.
- [3] T. DebRoy, H.L. Wei, J.S. Zuback, T. Mukherjee, J.W. Elmer, J.O. Milewski, A.M. Beese, A. Wilson-Heid, A. De, W. Zhang, Additive manufacturing of metallic components – process, structure and properties, *Prog. Mater. Sci.* 92 (2018) 112–224, <https://doi.org/10.1016/j.pmatsci.2017.10.001>.
- [4] S. Thapliyal, M. Komarasamy, S. Shukla, L. Zhou, H. Hyer, S. Park, Y. Sohn, R.S. Mishra, An integrated computational materials engineering-anchored closed-loop method for design of aluminum alloys for additive manufacturing, *Materialia* (2019) 100574, <https://doi.org/10.1016/j.mtla.2019.100574>.
- [5] D.B. Miracle, O.N. Senkov, A critical review of high entropy alloys and related concepts, *Acta Mater.* 122 (2017) 448–511, <https://doi.org/10.1016/j.actamat.2016.08.081>.
- [6] D.B. Miracle, Critical Assessment, Critical assessment 14: high entropy alloys and their development as structural materials, *Mater. Sci. Technol.* (United Kingdom) 31 (2015) 1142–1147, <https://doi.org/10.1179/1743284714Y.0000000749>.
- [7] Y. Brif, M. Thomas, I. Todd, The use of high-entropy alloys in additive manufacturing, *Scr. Mater.* 99 (2015) 93–96, <https://doi.org/10.1016/j.scriptamat.2014.11.037>.
- [8] K. Kuwabara, H. Shiratori, T. Fujieda, K. Yamanaka, Y. Koizumi, A. Chiba, Mechanical and corrosion properties of AlCoCrFeNi high-entropy alloy fabricated with selective electron beam melting, *Addit. Manuf.* 23 (2018) 264–271, <https://doi.org/10.1016/j.addma.2018.06.006>.
- [9] A. Piglione, B. Dovgyy, C. Liu, C.M. Gourlay, P.A. Hooper, M.S. Pham, Printability and microstructure of the CoCrFeMnNi high-entropy alloy fabricated by laser powder bed fusion, *Mater. Lett.* 224 (2018) 22–25, <https://doi.org/10.1016/j.matlet.2018.04.052>.
- [10] Z. Li, K.G. Pradeep, Y. Deng, D. Raabe, C.C. Tasan, Metastable high-entropy dual-phase alloys overcome the strength-ductility trade-off, *Nature* 534 (2016) 227–230, <https://doi.org/10.1038/nature17981>.
- [11] S.S. Nene, M. Frank, K. Liu, R.S. Mishra, B.A. McWilliams, K.C. Cho, Extremely high strength and work hardening ability in a metastable high entropy alloy, *Sci. Rep.* 8 (2018) 1–8, <https://doi.org/10.1038/s41598-018-28383-0>.
- [12] S.S. Nene, K. Liu, M. Frank, R.S. Mishra, R.E. Brennan, K.C. Cho, Z. Li, D. Raabe, Enhanced strength and ductility in a friction stir processing engineered dual phase high entropy alloy, *Sci. Rep.* 7 (2017) 1–7, <https://doi.org/10.1038/s41598-017-16509-9>.
- [13] E.I. Galindo-Nava, P.E.J. Rivera-Díaz-del-Castillo, Understanding martensite and twin formation in austenitic steels: a model describing TRIP and TWIP effects, *Acta Mater.* 128 (2017) 120–134, <https://doi.org/10.1016/j.actamat.2017.02.004>.
- [14] Z. Li, A. Ludwig, A. Savan, H. Springer, D. Raabe, Combinatorial metallurgical synthesis and processing of high entropy alloys, *J. Mater. Res.* 33 (2018) 3156–3169, <https://doi.org/10.1557/jmr.2018.214>.
- [15] J. Liu, X. Guo, Q. Lin, Z. He, X. An, L. Li, P.K. Liaw, X. Liao, L. Yu, J. Lin, L. Xie, J. Ren, Y. Zhang, Excellent ductility and serration feature of metastable CoCrFeNi high-entropy alloy at extremely low temperatures, *Sci. China Mater.* 62 (2019) 853–863, <https://doi.org/10.1007/s40843-018-9373-y>.
- [16] S.S. Nene, M. Frank, K. Liu, S. Sinha, R.S. Mishra, B. McWilliams, K.C. Cho, Reversed strength-ductility relationship in microstructurally flexible high entropy alloy, *Scr. Mater.* 154 (2018) 163–167, <https://doi.org/10.1016/j.scriptamat.2018.05.043>.
- [17] K. Liu, S.S. Nene, M. Frank, S. Sinha, R.S. Mishra, Extremely high fatigue resistance in an ultrafine grained high entropy alloy, *Appl. Mater. Today* 15 (2019) 525–530, <https://doi.org/10.1016/j.apmt.2019.04.001>.
- [18] A. Glage, A. Weidner, H. Biermann, Effect of austenite stability on the low cycle fatigue behavior and microstructure of high alloyed metastable austenitic cast TRIP-steels, *Procedia Eng.* 2 (2010) 2085–2094, <https://doi.org/10.1016/j.proeng.2010.03.224>.
- [19] W.E. Frazier, Metal additive manufacturing: a review, *J. Mater. Eng. Perform.* 23 (2014) 1917–1928, <https://doi.org/10.1007/s11665-014-0958-z>.
- [20] Z. Wang, T.A. Palmer, A.M. Beese, Effect of processing parameters on microstructure and tensile properties of austenitic stainless steel 304L made by directed energy deposition additive manufacturing, *Acta Mater.* 110 (2016) 226–235, <https://doi.org/10.1016/j.actamat.2016.03.019>.
- [21] T. Voisin, N.P. Calta, S. Khairallah, J.B. Forien, L. Balogh, R.W. Cunningham, A.D. Rollett, Y.M. Wang, Defects-dictated tensile properties of selective laser melted Ti-6Al-4V, *Mater. Des.* 158 (2018) 113–126, <https://doi.org/10.1016/j.matdes.2018.08.004>.
- [22] Z.C. Luo, M.X. Huang, Revealing the fracture mechanism of twinning-induced plasticity steels, *Steel Res. Int.* 89 (2018) 1–7, <https://doi.org/10.1002/srin.201700433>.
- [23] T.M. Mower, M.J. Long, Mechanical behavior of additive manufactured, powder-bed laser-fused materials, *Mater. Sci. Eng. A* 651 (2016) 198–213, <https://doi.org/10.1016/j.msea.2015.10.068>.
- [24] M. Linderov, C. Segel, A. Weidner, H. Biermann, A. Vinogradov, Deformation mechanisms in austenitic TRIP/TWIP steels at room and elevated temperature investigated by acoustic emission and scanning electron microscopy, *Mater. Sci. Eng. A* 597 (2014) 183–193, <https://doi.org/10.1016/j.msea.2013.12.094>.
- [25] S. Allain, J.P. Chateau, O. Bouaziz, S. Migot, N. Guelton, Correlations between the calculated stacking fault energy and the plasticity mechanisms in Fe-Mn-C alloys,

- Mater. Sci. Eng. A 387–389 (2004) 158–162, <https://doi.org/10.1016/j.msea.2004.01.059>.
- [26] Q. Lin, J. Liu, X. An, H. Wang, Y. Zhang, X. Liao, Cryogenic-deformation-induced phase transformation in an FeCoCrNi high-entropy alloy, Mater. Res. Lett. 6 (2018) 236–243, <https://doi.org/10.1080/21663831.2018.1434250>.
- [27] M. Frank, Y. Chen, S.S. Nene, S. Sinha, K. Liu, K. An, R.S. Mishra, Investigating the deformation mechanisms of a highly metastable high entropy alloy using in-situ neutron diffraction, Mater. Today Commun. 23 (2020) 100858, <https://doi.org/10.1016/j.mtcomm.2019.100858>.
- [28] S. Sinha, S.S. Nene, M. Frank, K. Liu, P. Agrawal, R.S. Mishra, On the evolving nature of c/a ratio in a hexagonal close-packed epsilon martensite phase in transformative high entropy alloys, Sci. Rep. 9 (2019) 1–14, <https://doi.org/10.1038/s41598-019-49904-5>.
- [29] D. Manfredi, F. Calignano, M. Krishnan, R. Canali, E.P. Ambrosio, S. Biamino, D. Ugues, M. Pavese, P. Fino, Light metal alloys applications, Light Met. Alloy. Appl. (2014) 3–34, <https://doi.org/10.5772/57069>.
- [30] P. Kumar, O. Prakash, U. Ramamurty, Micro-and meso-structures and their influence on mechanical properties of selectively laser melted Ti-6Al-4V, Acta Mater. 154 (2018) 246–260, <https://doi.org/10.1016/j.actamat.2018.05.044>.
- [31] Y. Zhai, H. Galarraga, D.A. Lados, Microstructure evolution, tensile properties, and fatigue damage mechanisms in Ti-6Al-4V alloys fabricated by two additive manufacturing techniques, Procedia Eng. 114 (2015) 658–666, <https://doi.org/10.1016/j.proeng.2015.08.007>.
- [32] S. Luo, C. Zhao, H. Yang, Q. Liu, Z. Wang, X. Zeng, Selective laser melting of dual phase AlCrCuFeNix high entropy alloys: formability, heterogeneous microstructures and deformation mechanisms, Addit. Manuf. (2019) 100925, <https://doi.org/10.1016/J.ADDMA.2019.100925>.
- [33] F. Peyrouzet, D. Hachet, R. Soulard, C. Navone, S. Godet, S. Gorsse, Selective laser melting of Al0.3CoCrFeNi high-entropy alloy: printability, microstructure, and mechanical properties, Jom. 71 (2019) 3443–3451, <https://doi.org/10.1007/s11837-019-03715-1>.
- [34] Z.G. Zhu, X.H. An, W.J. Lu, Z.M. Li, F.L. Ng, X.Z. Liao, U. Ramamurty, S.M.L. Nai, J. Wei, Selective laser melting enabling the hierarchically heterogeneous microstructure and excellent mechanical properties in an interstitial solute strengthened high entropy alloy, Mater. Res. Lett. 7 (2019) 453–459, <https://doi.org/10.1080/21663831.2019.1650131>.
- [35] L.E. Murr, E. Martinez, J. Hernandez, S. Collins, K.N. Amato, S.M. Gaytan, P.W. Shindo, Microstructures and properties of 17-4 PH stainless steel fabricated by selective laser melting, J. Mater. Res. Technol. 1 (2012) 167–177, [https://doi.org/10.1016/S2238-7854\(12\)70029-7](https://doi.org/10.1016/S2238-7854(12)70029-7).
- [36] A. Mertens, S. Reginster, H. Paydas, Q. Contrepois, T. Dormal, O. Lemaire, J. Lecomte-Beckers, Mechanical properties of alloy Ti-6Al-4V and of stainless steel 316L processed by selective laser melting: influence of out-of-equilibrium microstructures, Powder Metall. 57 (2014) 184–189, <https://doi.org/10.1179/174329014Y.0000000092>.
- [37] K. Abd-Elghany, D. Bourell, Property evaluation of 304L stainless steel fabricated by selective laser melting, Rapid Prototyp. J. 18 (2012) 420–428, <https://doi.org/10.1108/13552541211250418>.
- [38] J. Mazumder, J. Choi, K. Nagarthanam, J. Koch, D. Hetzner, The direct metal deposition of H13 tool steel for 3D components, J. Met. 49 (1997) 55–60, <https://doi.org/10.1007/BF02914687>.
- [39] K.G. Prashanth, S. Scudino, H.J. Klauss, K.B. Surreddi, L. Löber, Z. Wang, A.K. Chaubey, U. Kühn, J. Eckert, Microstructure and mechanical properties of Al-12Si produced by selective laser melting: effect of heat treatment, Mater. Sci. Eng. A 590 (2014) 153–160, <https://doi.org/10.1016/j.msea.2013.10.023>.
- [40] A. Barbas, A.S. Bonnet, P. Lipinski, R. Pesci, G. Dubois, Development and mechanical characterization of porous titanium bone substitutes, J. Mech. Behav. Biomed. Mater. 9 (2012) 34–44, <https://doi.org/10.1016/j.jmbbm.2012.01.008>.